ChemPhysChem

Research Article
doi.org/10.1002/cphc.202400154

Chemistry Europe
European Chemical
Societies Publishing

www.chemphyschem.org

Chitosan as Support Material for Metal-Organic Framework based Catalysts

Christia R. Jabbour,[a] Kordula B. Schnabl,[a] Haoxiang Yan,[a] Naoise N. O'Beirn,[a] Joren M. Dorresteijn,[a] Florian Meirer,[a] Laurens D. B. Mandemaker,*[a] and Bert M. Weckhuysen*[a]

Turning waste into valuable products is one of the main challenges of the chemical industry. In this work, chitosan (CS), an abundant, low-cost, and non-toxic biopolymer derived from chitin, was reshaped into beads of ~3 mm. Their suitability as a support material for active phase catalyst materials was tested for a zirconium-based Metal-Organic Framework (MOF) with incorporated Pt, namely UiO-67-Pt. Its incorporation was investigated via two procedures: a one-pot synthesis (OPS) and a post-synthetic functionalization (PSF) synthesis method. Scanning electron microscopy (SEM) images show good UiO-67-Pt dispersion throughout the CS beads for the one-pot synthesized material (UiO-67-Pt-OPS@CS). However, this uniform dispersion was not observed for the post-synthetically functionalized material (UiO-67-Pt-PSF@CS). The success of the implementation of UiO-67-Pt was evaluated with ultraviolet-visible and infrared spectroscopy for both composite materials. Thermogravimetric analysis (TGA) reveals higher thermal stabilities for UiO-67-Pt-OPS@CS composite beads in comparison to pure CS beads, but not for UiO-67-Pt-PSF@CS. The study provides valuable insights into the potential of chitosan as a green, bead-shaped support material for MOFs, offering flexibility in their incorporation through different synthesis routes. It further contributes to the broader goal of the sustainable and eco-friendly design of a new generation of catalysts made from waste materials, which will be the topic of future studies.

Introduction

The application of metal-organic frameworks (MOFs) has gained a lot of attention due to their unique structure and versatile properties, which makes them suitable to catalyze a myriad of chemical reactions.[1,2] Due to their highly porous character and great tunability, resulting from their inorganic-organic bonds between metal ions and organic linkers, they can be adjusted in their functional, structural, and compositional properties.[3] This great tunability makes them highly versatile for distinct applications, like for example in the adsorption and conversion of carbon dioxide (CO_2), a key greenhouse gas, into valuable chemical products, such as methanol.[4–8]

Platinum-based catalysts have demonstrated their potential in the hydrogenation of CO_2 into valuable chemicals.[9–11] For example, Gutterod et al.[12] studied CO_2 hydrogenation over a platinum-containing UiO-67 MOF, belonging to the UiO zirconium-based MOF series, and compared its performance to that of a pure platinum on silica (Pt/SiO_2) catalyst. Their findings indicate that the activation energy for both catalyst materials is similar, but the Pt-containing UiO-67 catalyst exhibits a tendency to achieve a higher turnover frequency compared to Pt/SiO_2.

The development of an effective catalyst material for any specific chemical reaction holds significant importance for its extensive use on a large scale.[7,8,12–15] Hence, in industrial applications the preference for heterogeneous catalysis, as opposed to homogeneous catalysis, is primarily driven by several key factors, with the foremost being its stability, reusability, and relative ease for large-scale implementation.[16,17]

In many industrial processes, the catalyst material is typically shaped from its powder form into various bodies, such as extrudates, beads, or monoliths. This shaping of the catalyst material not only enables smoother reactant and product flow within the catalyst bed but also mitigates pressure drop within chemical reactors. Consequently, it enhances mass transport within the catalyst material, ultimately bolstering its overall catalytic performance during the process.[18–20] However, for a significant portion of industrially applied catalysts, the process and impact of shaping can harm their mechanical stability and can lead to poor catalytic performance.[19–23] When it comes to certain MOFs, the application of mechanical pressure to convert powders into solid bodies can lead to partial damage of the MOF structure. This could potentially have a detrimental effect on the catalyst porosity, leading to a decrease in its activity. In research reported by Su et al.,[24] it was demonstrated that subjecting UiO-66 to bulk compression at pressures between 1.9 and 4.0 GPa leads to the disintegration of the chemical bond between the metal and the linker, resulting in a gradual

[a] C. R. Jabbour,+ K. B. Schnabl,+ H. Yan, N. N. O'Beirn, J. M. Dorresteijn, Dr. F. Meirer, Dr. L. D. B. Mandemaker, Prof. Dr. B. M. Weckhuysen
Inorganic Chemistry and Catalysis group, Debye Institute for Nanomaterials Science and Institute for Sustainable and Circular Chemistry, Utrecht University, Universiteitsweg 99, 3584 CG Utrecht (The Netherlands)
E-mail: L.D.B.Mandemaker@uu.nl
B.M.Weckhuysen@uu.nl

ChemPhysChem

Research Article
doi.org/10.1002/cphc.202400154

Chemistry Europe
European Chemical
Societies Publishing

decrease in the number of Zr–O bonds between Zr(IV) ions and the carboxylate groups.

As an alternative to catalyst pelletization or extrusion, a carrier or support material can be employed to avoid the need to apply mechanical pressure for the shaping process. Within this context, biopolymers have gained growing popularity as potential carrier materials in a wide range of applications, primarily due to their attractive properties, such as biocompatibility, biodegradability, and sustainability.[25,26] There is a growing interest in repurposing renewable alternatives that are currently predominantly treated as waste, typically ending up in landfills or being discarded into the sea.[27,28] One of these biomass-based alternatives studied worldwide is chitin, the second most abundant biopolymer after cellulose, which is mainly obtained from the shells of crustaceans, such as shrimp, crabs, and lobsters.[29,30] However, due to its stability, natural decomposition takes years if not treated otherwise, and it is in general very challenging to dissolve.[31] To enhance its industrial viability, chitin is often transformed into chitosan (CS) by (partial) deacetylation, increasing its solubility and therefore workability of the polymer.[29,30,32–34] The intrinsic properties of

chitosan being non-toxic, biodegradable, biocompatible, and antimicrobial are additional advantages, making it a versatile material that finds applications in diverse fields, such as biomedicine, pharmaceuticals, food industry, green chemistry, and catalysis.[33–40] Previously, chitosan has been employed as a support material for metal catalysts in a variety of organic transformations,[41] within chitosan-based catalytic systems in the synthesis of heterocyclic rings,[42] and in biomedical contexts for enzyme immobilization.[43] Nonetheless, none of these presented studies explored the potential of integrating MOFs, which offer exceptional adaptability as catalysts.

In this study, chitosan powder was reshaped into beads to serve as a carrier material for a MOF catalyst materials, namely Pt nanoparticles supported on the zirconium-based MOF UiO-67 (UiO-67-Pt), built from $Zr_6O_4(OH)_4$ clusters connected by 1-1'-biphenyl-4,4'-dicarboxylic acid (BPDC) linker molecules.[3] The incorporation of UiO-67-Pt into these CS beads was achieved through two different synthesis methods, as schematically outlined in Figure 1. The objective of this research is to explore diverse synthesis methods enabling the creation of robust catalysts supported on environmentally friendly materials like
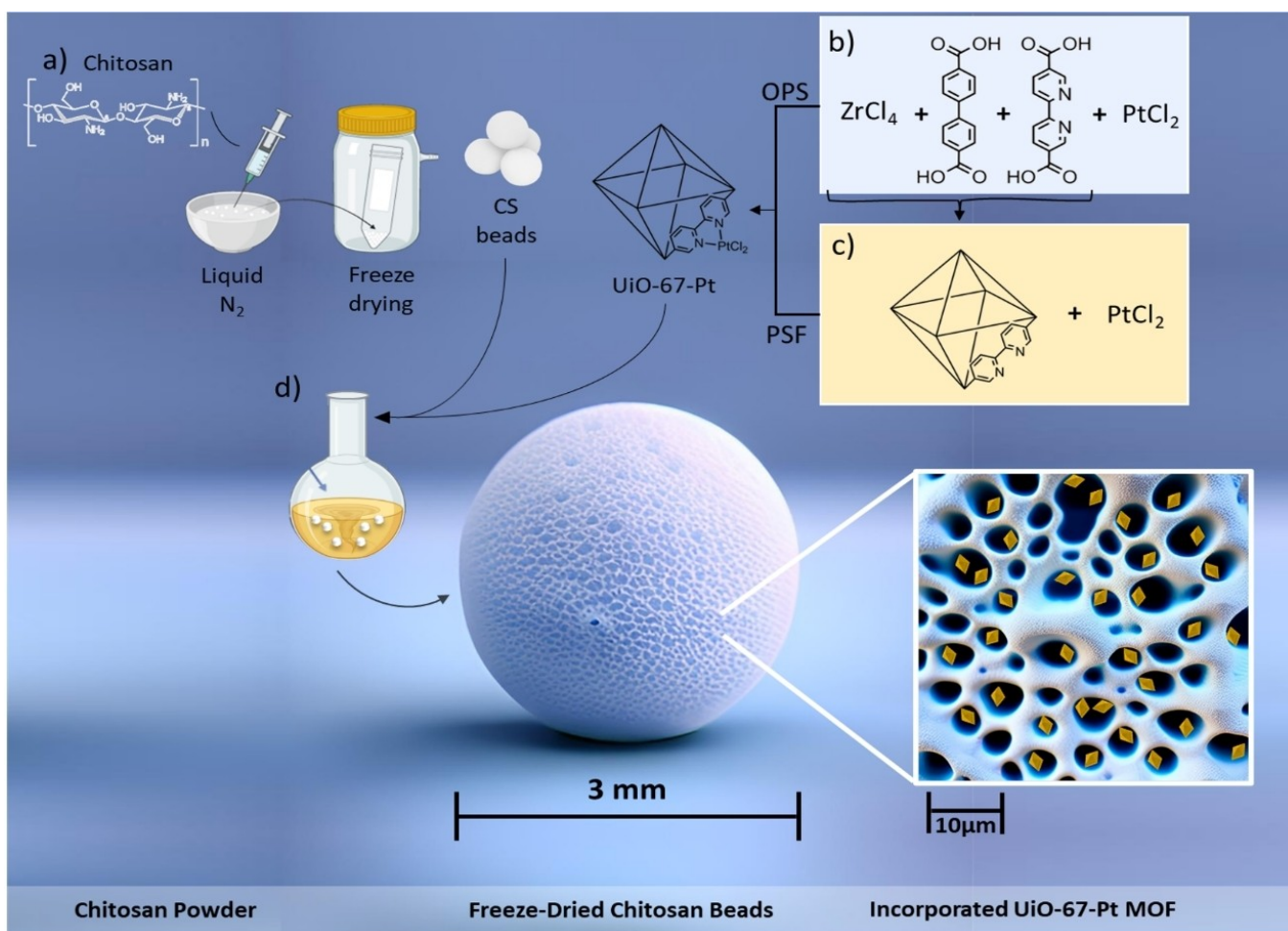

Figure 1. Schematic representation of the synthesis of chitosan (CS) beads by a) dissolving chitosan powder in acetic acid and drop casting them in liquid N_2. After freeze drying, pure CS beads were synthesized, which are then combined with b) UiO-67-Pt synthesized via the one-pot synthesis (OPS) or c) UiO-67-Pt synthesized via post-synthetic functionalization (PSF). After combining them in solution d), UiO-67-Pt was found on the bead surface and in the pores as schematically represented in e) where MOF crystals are represented in yellow.
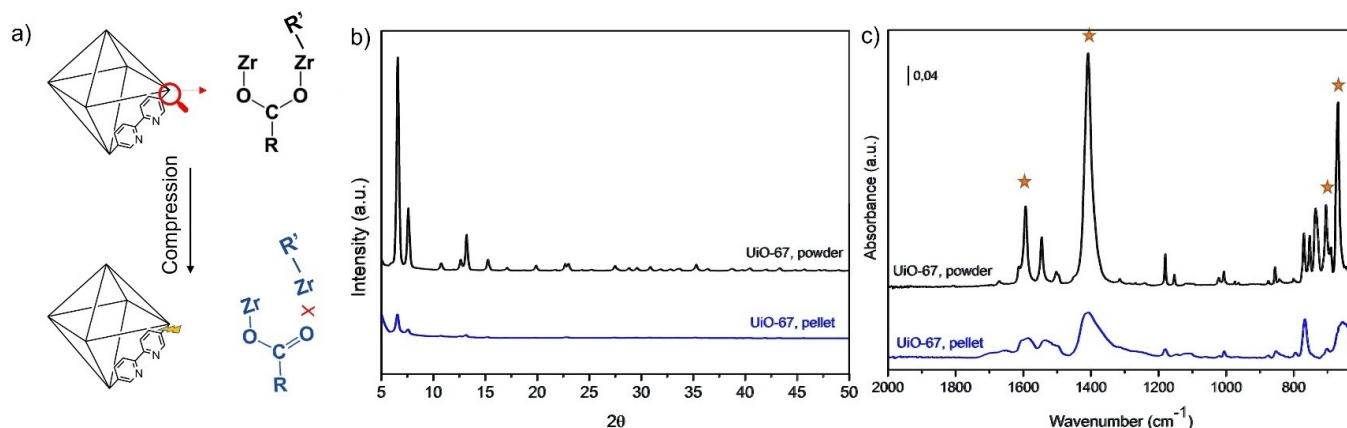
ChemPhysChem

Research Article
doi.org/10.1002/cphc.202400154

**Chemistry
Europe**
European Chemical
Societies Publishing

Figure 2. a) Illustration depicting the UiO-67 lattice in its original state (black) and subsequent to pelletization (blue). This visual highlights the chemical bond disruptions resulting from the application of pressure during the pelletization process. b) X-Ray diffraction (XRD) patterns of UiO-67 in its powder form before (black) and after (blue) palletization. c) Attenuated Total Reflection-Infrared (ATR-IR) spectra of a UiO-67 in its powder form before pelletization (black) and after (blue).

chitosan, all without the necessity of employing mechanical pressure during their fabrication. Follow-up research work will then focus on the application of these materials in various catalytic applications.

Results and Discussion

To highlight the sensitivity of the MOF structure to mechanical pressure, as was also reported by Su et al.,[24] we conducted a similar investigation by assessing the influence of a pelletization process on a UiO-67 sample by applying mechanical pressure of 1.52×10^{-4} GPa. The crystallinity of the pressed sample was evaluated using X-ray diffraction (XRD), whereas the chemical nature of the metal-linker bonds was analyzed using attenuated total reflection-infrared (ATR-IR) spectroscopy. In Figure 2a, an illustration presents a UiO-67 lattice in its original state (in black) and after pelletization (in blue), unveiling a break in the bond between the metal and the linker due to applied pressure. The XRD results, shown in Figure 2b, indicate a significant reduction in the sample crystallinity when comparing the powdered sample shown in Figure 2c, with the pelletized sample. Mainly, the symmetric and asymmetric stretching vibration of the C–O bond, respectively, broaden and decrease in their intensity after pelletization.[44] The same can be noted for the IR peaks at ~670 cm^{-1} and 770 cm^{-1}, which correspond to Zr–O vibrations.[45] In parallel, a broader peak emerges from ~1620 to 1720 cm^{-1}, which is due to the uncoordinated acid group of the linker, namely C=O, being formed upon the breaking of the Zr–O bond. These observations imply that (on average) the coordination between the linker and zirconia is both decreased and weakened, which is in line with the observed decrease in peak intensities in the XRD patterns. Hence, this susceptibility towards mechanical pressure motivates the idea of applying CS beads as carrier material to generate MOF-based catalyst materials.

The synthesis of pure CS beads involved drop-casting of a homogeneous acidic chitosan solution into liquid nitrogen, followed by freeze drying to remove any solvent from the beads (Figure 1a). The acidic chitosan solution was exclusively drop cast into liquid nitrogen using a BD microlance™ 3 needle, 0.8×40 mm in size. Tests were also made with lower concentrations of chitosan, as well as a smaller needle diameter (0.25×40 mm) to investigate the tunability of the bead size (Figure 3). Both variations lead to smaller beads. The formed beads were collected and freeze-dried for 24 h. in this work, the beads that were used as a support material for the incorporation of MOF material were made using the microlance needle with a 0.8 mm diameter.

Following the formation of CS beads, the incorporation of the catalyst UiO-67-Pt was done by exploring two different synthesis procedures: the one-pot synthesis (OPS) (Figure 1b) and the post-synthetic functionalization (PSF) route (Figure 1c).[46] Within the OPS route, the metal and linker precursors are added at the same time as the Pt salt, so the MOF forms directly on/in the chitosan bead. In contrast, PSF is a two-step approach, in which first the UiO-67 is made from the zirconium metal clusters and linkers. In a second step, the MOF powders
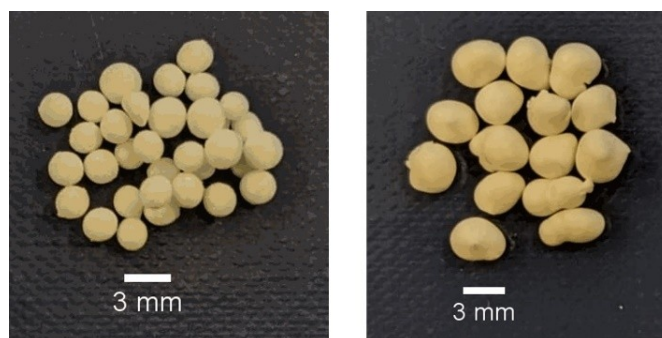

Figure 3. Chitosan bead size dependance using a BD microlance™ left: 0.25 mm diameter needle and right: 0.8 mm diameter.

ChemPhysChem

Research Article
doi.org/10.1002/cphc.202400154

Chemistry Europe
European Chemical
Societies Publishing

are mixed with the chitosan beads and the Pt salt in solution, allowing the MOF to be impregnated by the Pt salt and at the same time let diffuse the MOF crystals into the larger, porous chitosan beads. The synthesis method employed for UiO-67-Pt, whether it is through OPS or PSF, does not affect its crystallinity. Figure S1 demonstrates similar diffractograms for UiO-67-Pt synthesized via the OPS route (UiO-67-Pt-OPS) and PSF (UiO-67-Pt-PSF). In this work, we have used the abbreviations UiO-67-Pt-OPS@CS and UiO-67-Pt-PSF@CS, thereby referring to the beads with incorporated MOF, referencing the synthesis method used to incorporate the catalytically active UiO-67-Pt material.

The pure CS beads as well as both synthesis pathways for the composite materials resulted in beads measuring 3 mm in diameter, with a sponge-like texture, as can be seen in Figure 4a. To investigate the beads in more detail, scanning electron microscopy (SEM) was used to monitor the physical change of the beads before and after the incorporation of the MOF on the outer bead surface (Figure 4b) as well as on the inner surface after cutting the bead open (Figure 4c). The outer and inner surfaces of the pure CS beads (white, top row), UiO-67-Pt-OPS@CS beads (blue, middle row), and architecture of the CS beads allows effective interaction with the MOF.

The synthesis method for UiO-67-Pt-OPS@CS beads involves the chemical growth of UiO-67-Pt crystals on both the outer shell and within the pores of the CS beads. Figure 4 shows consistency in the distribution of UiO-67-Pt crystals on both the external and internal surfaces of the CS bead. As for the UiO-67-Pt-PSF@CS beads, both the outer and inner surfaces of the CS bead show to have more of a flaky plate-like structure. Nevertheless, some MOF crystals migrated towards the inside of the bead due to the stirring of the MOF powder (1000 rpm) with the pure CS beads while impregnating (Figure S2).

UiO-67-Pt-PSF@CS (orange, bottom row) all display a very porous structure throughout their composition. Upon closer examination, the SEM images of the UiO-67-Pt-OPS@CS sample reveal the formation of a surface-anchored MOF film on parts of the CS bead. Figure 5 shows the formation of such a UiO-67-Pt sheet-like film. Typically, a MOF film is formed by anchoring on a substrate, where the film thickness, homogeneity, morphology, and dimensions are affected by the type of substrate in use.[47,48]

In this case, the CS bead acts as a substrate for UiO-67-Pt, possibly as the N—H or O—H groups of chitosan can act as initial anchoring points for the first "cycle" of zirconium metal clusters to bind. Figure 5a shows a layer of material forming on the surface of the CS bead with different particle size distributions of crystallites. Throughout the synthesis, these crystallites seem to merge to MOF film, as indicated by a red arrow in Figure 5b. This growth mechanism is indicative of a Volmer–Weber-type growth.[49] The formation of the UiO-67 film on the CS bead was only observed for the composites made via the OPS route. It appears, form Figure 5b, that the MOF octahedral crystals are anchored in either the (100) or (111) orientation. However, there's a noticeable preference for the (111) orientation.[50]
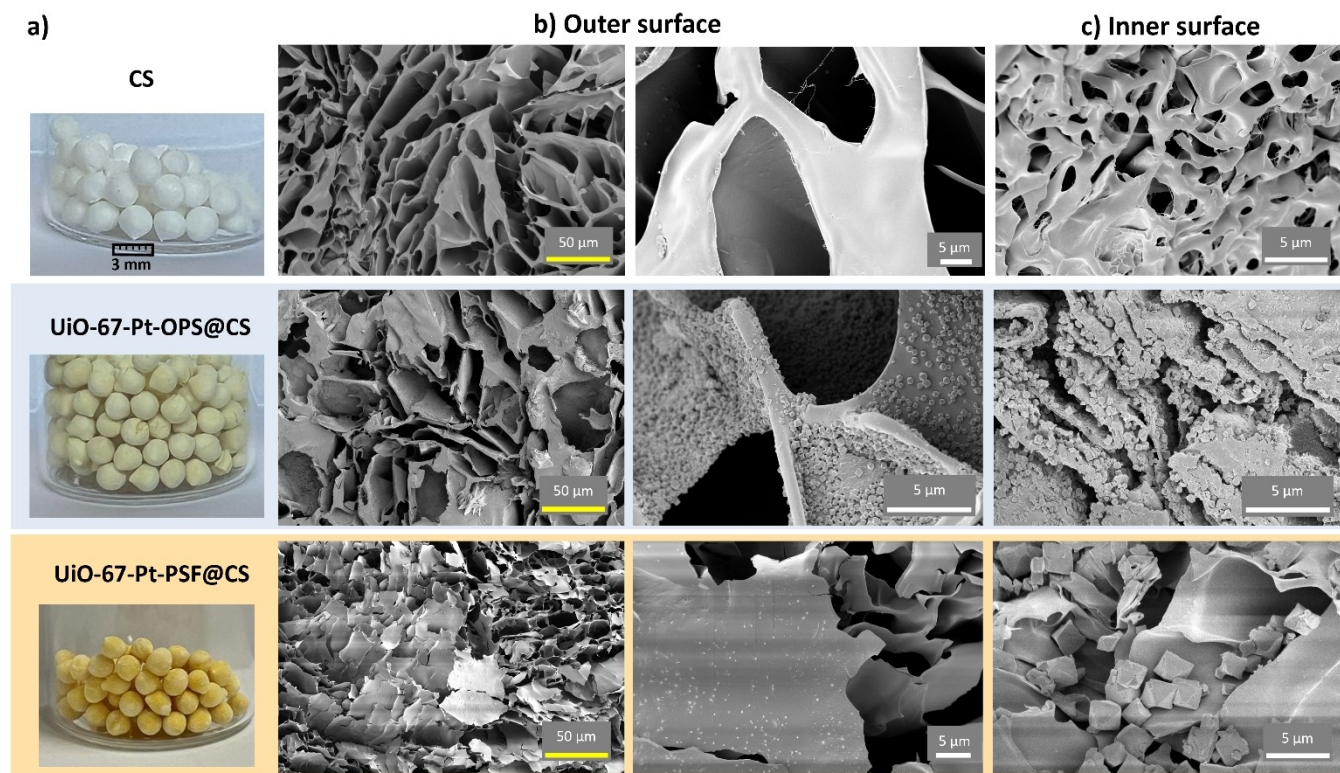

Figure 4. Visual overview of CS (top), UiO-67-Pt-OPS@CS (blue, middle), and UiO-67-Pt-PSF@CS (orange, bottom) beads; a) Photos of the beads, 3 mm in diameter in size each synthesized using BD microlance™ 3 needle, 0.8×40 mm in size. Scanning Electron Microscopy (SEM) images of b) the outer surface and c) the inner surface of the beads after cutting them in half. The yellow scale bar indicates 50 μm and the white bar 5 μm.
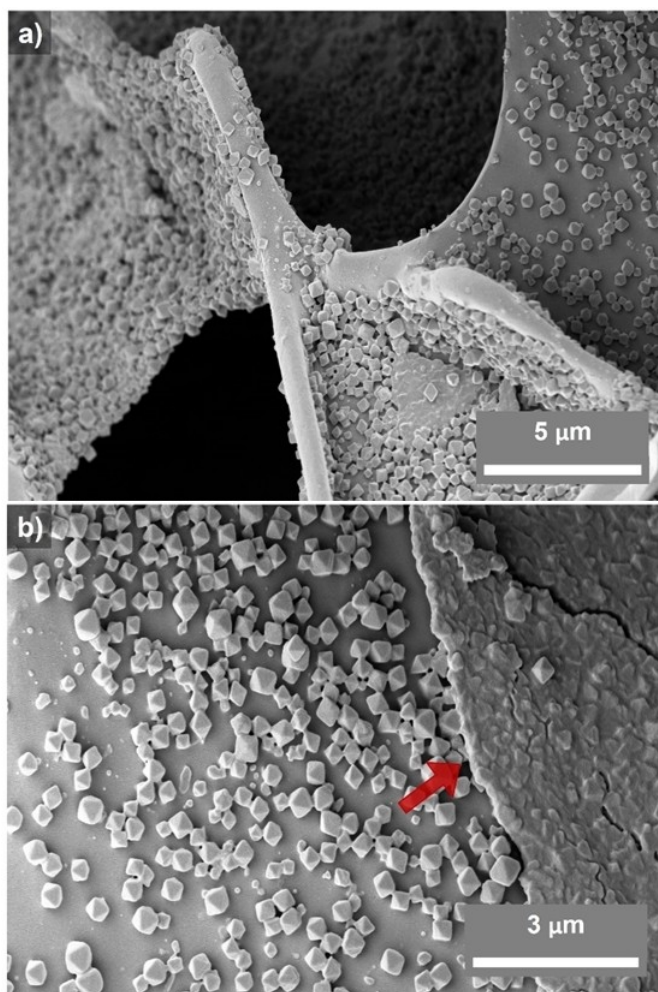
ChemPhysChem

Research Article
doi.org/10.1002/cphc.202400154

Chemistry
Europe
European Chemical
Societies Publishing

Figure 5. Scanning Electron Microscopy (SEM) images of UiO-67-Pt-OPS@CS a) an overview of the outer surface of the composite bead, and b) a zoom-in showing the individual crystallites as well as the intergrown MOF layer.

Finally, to gain more understanding on the effect of the MOF incorporation on the pore size of the bead, mercury (Hg) porosimetry was measured on the beads as shown in Figure S3. N_2 physisorption on these hybrid materials is extremely challenging due to the different MOF loadings and broad variety of pore sizes, combined with the spherical geometry of the sample. Hence, Hg porosimetry was used to at least observe changes in the larger pores of the chitosan beads. As can be seen from the cumulative intrusion profiles in Figure S3, it seems that incorporation of the MOF leads to lower cumulative intrusion. The total intrusion volume, as shown in the inset table in Figure S3, demonstrates that the beads undergo a reduction in pore volume significantly when using the OPS method. This is in line with the observations done with SEM, as shown in Figure 4, in which OPS featured MOF crystals and film within the inner bead. Interestingly, the intrusion volume after applying the PSF method is unchanged compared to the pristine beads, which hints at a low amount of MOF present using this method and will be elaborated on *vide infra*. The median pore diameter, calculated from the pressure and pore volume in which 50% of the total volume was added, decreases

from 28,33 μm for the pristine beads to 9,078 μm (PSF) and 7,45 μm (OPS) after MOF incorporation. We argue that the decrease for the PSF method, together with the hardly unchanged total intrusion volume, is due to the high loading of MOF and thus strong pore decrease in the outer shell of the beads, whereas for OPS it can be expected that the found pore diameter is more representative for the total bead, resulting in the significantly lower total intrusion volume. From this we can conclude that first of all, the beads exhibit μm-sized pores that are not fully blocked upon the introduction of MOFs. But second, we can conclude that as the total intrusion volume for the OPS method decreased significantly, the loading of the MOF throughout the bead was higher and more uniform than for the PSF method.

ICP analysis was conducted on both chitosan (CS) beads and composite beads (UiO-67-Pt-OPS@CS and UiO-67-Pt-PSF@CS). The findings revealed that Pt content in the composite beads synthesized via PSF was 3.5 times greater than that in beads synthesized via OPS. This suggests that more Pt attaches to the CS beads during the PSF synthesis route. Conversely, Zr content was found to be 7 times higher in composite beads synthesized via OPS compared to PSF, indicating a greater presence of MOF material in UiO-67-Pt-OPS@CS (Table S1). These findings correlate with the synthesis route employed. However, it is important to mention that dissolving the MOFs for ICP analysis using standard acids is challenging, as the material is well known to be rather stable in such media. Hence, we can only qualitatively compare the different materials here and do not want to make claims on the quantitative amounts of Zr and Pt within the beads.

Due to the stark contrast of the beads in their color, we have investigated the different CS beads and powders using Ultraviolet-Visible (UV-Vis) spectroscopy (Figure S4). It was found that the UiO-67-Pt-PSF@CS beads absorb light at higher wavelengths and therefore are perceived as more orange than the UiO-67-Pt-OPS@CS beads. As K_2PtCl_4 is known to link to chitosan and absorb at wavelength up to ~400 nm,[51] this indicates a competitive uptake of the Pt salt on the chitosan as well as on the MOF. This results in a higher total Pt amount in the beads in comparison to the pure MOF powders (Figure S4a and S4b). A similar trend is observed for the powder samples: UiO-67-Pt-OPS absorbs a greater amount of Pt-salt than UiO-67-Pt-PSF (Figure S4c).

The chemical composition of the composite beads was analyzed using ATR-IR spectroscopy and the results are shown in Figure 6. The IR peaks located at ~670 and ~770 cm^{-1} correspond to the transverse and the longitudinal vibrational modes of the Zr–O bond in the MOF unit.[52,53] The intense IR peaks located at ~1410 and ~1600 cm^{-1} are the symmetric and symmetric stretching vibrations of the COO- groups, respectively, representing the linker bound with both oxygen atoms.[45,54–57] The IR peak located at ~1670 cm^{-1} for UiO-67-Pt synthesized via the OPS route, corresponds to uncoordinated linker C═O stretching, which is a characteristic of unbound linker groups. This IR peak indicates the presence of either partially uncoordinated linkers in the structure or the presence of free, totally unreacted linkers.[52] The IR peak located at
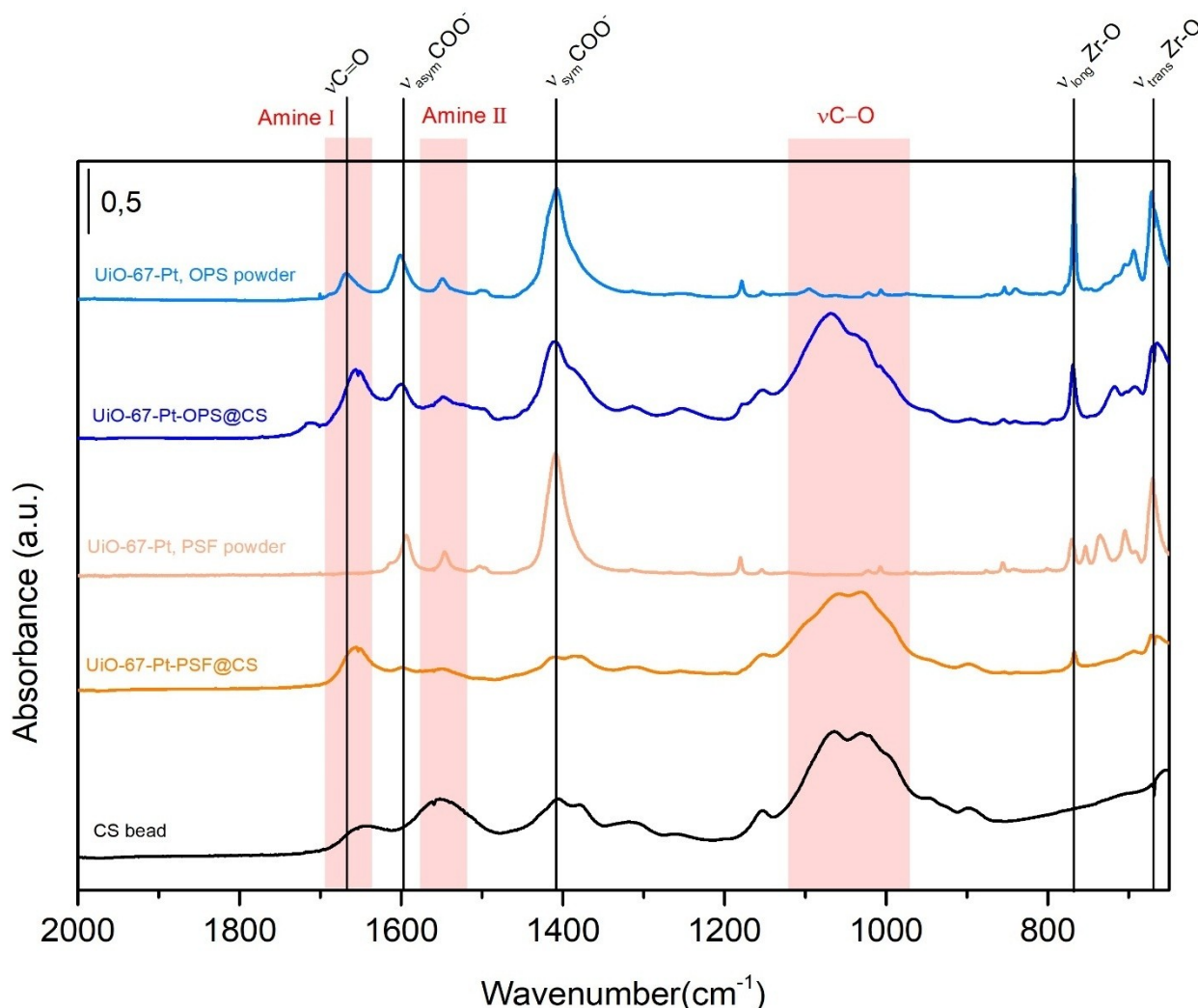
ChemPhysChem

Research Article
doi.org/10.1002/cphc.202400154

Chemistry Europe
European Chemical
Societies Publishing

Figure 6. Attenuated total reflection-infrared (ATR-IR) zoom-in spectra of a UiO-67-Pt-OPS powder (light blue), UiO-67-Pt-OPS@CS bead (dark blue), UiO-67-Pt-PSF powder (light orange), UiO-67-Pt-PSF@CS bead (dark orange) and CS bead (black). The bands that are highlighted serve to showcase the distinctive features of chitosan, while the black line denotes peaks associated with the MOF.

~1550 cm^{-1} of the UiO-67-Pt samples, belongs to the C–C ring vibration mode.

The IR fingerprint of the chitosan bead appears to closely resemble that of the chitosan powder, underlining the purity of the beads (Figure S5). The broad IR peak located at ~1025 cm^{-1} is related to the C–O skeletal stretching vibration of chitosan, which is found to be present in the chitosan bead and chitosan powder. The IR peaks located at ~1650 cm^{-1} and ~1550 cm^{-1} belong to the primary and secondary amide groups present in chitosan,[58,59] while the IR peak located at ~1550 cm^{-1} is the most prominent for the pure CS beads and the IR peak located at ~1650 cm^{-1} is more intense for the UiO-67-Pt-OPS@CS composite beads. The latter IR peak corresponds to the carbonyl groups of the unreacted linker groups in the MOF, which form bonds with the amine group of the CS (i.e., a C=O-NHR functionality).[60] However, for the UiO-67-Pt-PSF@CS composite sample, the IR peaks located at ~1400 cm^{-1} and ~1050 cm^{-1} represent the CS vibrations, which are most prominent, and the expected coordinated linker or Zr–O peaks

are hardly visible, underlining that there is most likely not much MOF material within the composite bead.

To test the thermal stability of the beads and to confirm the co-existence of the MOF in both composite materials, Thermogravimetric Analysis (TGA) was used. Figure 7 summarizes the obtained TGA data where the weight loss curves are shown in the left panels with dashed lines, while their 1st derivatives are shown in the right panels with solid lines. For the CS bead (black) we found an initial weight loss (first peak in first derivative at ~120 °C), which results from water. Additionally, the TGA data show a clear degradation temperature, which is located at ~290 °C only 10 °C lower than the degradation temperature of chitosan powder (grey; Figure 7e, f).

The UiO-67-Pt-OPS material (light blue, denoted with "x") shows an initial decrease in weight (broad peak in the 1st derivative at ~150 °C) which is shown in the literature to arise from free linkers in the MOF.[61] The second peak located at ~573 °C is related to the degradation of the MOF itself. This is also clearly visible for the weight-loss curve and its 1st derivative

ChemPhysChem

Research Article
doi.org/10.1002/cphc.202400154

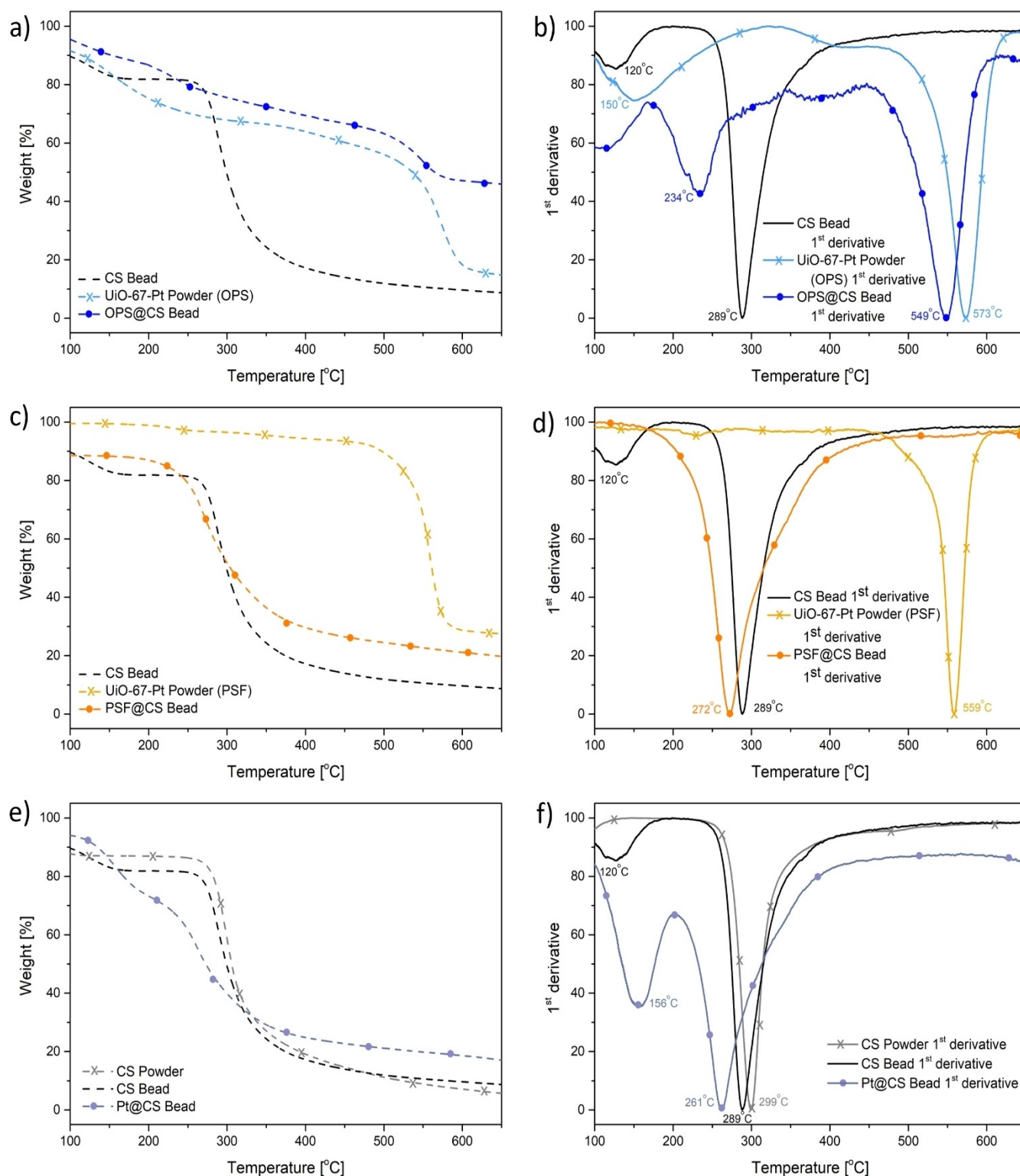**Chemistry
Europe**
European Chemical
Societies Publishing

Figure 7. Thermogravimetric Analysis (TGA) weight loss curves (dashed lines; a),c),and e)) and their respective first derivatives (solid lines; b,d,f) of a a,b) pure chitosan beads (black), UiO-67-Pt-OPS powder (light blue, with symbol "x"), UiO67-Pt-OPS@CS bead (dark blue, with symbol "●"); c,d) pure chitosan beads (black), UiO-67-Pt-PSF powder (light orange, with symbol "x"), and UiO67-Pt PSF@CS bead (dark orange, with symbol "●"); e,f) pure chitosan bead (black), pure chitosan power (grey, with symbol "x"), and chitosan beads impregnated with Pt salt (blue-grey, with symbol "●").

of the UiO-67-Pt- OPS@CS bead, for which the maximum weight loss temperature shown in the minimum of the 1ˢᵗ derivative is shifted to a lower temperature at ~549 °C (Figure 7a, b). Similar

to the UiO-67-Pt-OPS material, UiO-67-Pt-PSF degrades at ~560 °C (Figure 7c, d). However, the UiO-67-Pt-PSF@CS beads (dark orange, denoted with "●") fully degrade even at slightly

ChemPhysChem

Research Article
doi.org/10.1002/cphc.202400154

Chemistry Europe
European Chemical
Societies Publishing

lower temperatures than the pure CS beads, at ~272 °C. Apart from a slight peak in the 1st derivative, occurring at ~560 °C (dark orange), we do not detect any noticeable MOF-related weight loss within the weight loss curve of the UiO-67-Pt-PSF@CS beads. These results further indicate free linkers being available in the MOFs from the OPS beads, whereas for the PSF beads nearly no MOF was formed on/in the bead. Given that an intact MOF typically exhibits a degradation temperature of approximately 560 °C, it appears that during the synthesis of the UiO-67-Pt-PSF@CS beads, the initially synthesized MOF might have either fallen off while forming the composite material or was not properly attached to the CS beads. Post TGA analysis were conducted on both the pure CS bead and UiO-67-Pt-OPS@CS. Figure S8 illustrates the visual inspection following the TGA analysis, revealing beads with a semi-spherical shape but displaying reduced physical stability. Additionally, IR spectra were recorded before and after TGA analysis for both samples, revealing a complete loss of chemical structure in both cases.

Conclusions

A chitosan-based composite has been developed as a potential porous material for supporting metal-organic framework (MOF)-based catalyst materials. The direct one-pot synthesis (OPS) method to form the MOF inside the chitosan carrier results in superior physicochemical properties as compared to the indirect post-synthetic functionalization (PSF) method, meaning that the OPS method is the favorable synthesis route. The incorporation of the UiO-67-Pt material via the OPS route also showed a more promising approach in terms of the amount and the stability of the integrated UiO-67-Pt-MOF crystals. A Volmer–Weber-based growth mechanism was observed for the UiO-67-Pt-OPS@CS composites, meaning that a MOF film was synthesized on the large pore walls of the chitosan bead instead of individual particles. This holds potential to bring the enhanced properties of MOF films into the field of heterogeneous catalysis.

The incorporation of the MOF materials into the chitosan-based beads through the PSF method resulted in a heterogeneous diffusion of the MOF crystals, where they were mostly found located on the outside of the chitosan beads. Furthermore, we observed a lower presence of unbound linkers within the structure of composite materials produced via the PSF route compared to those produced via the OPS method. The significance of these unbound linkers in anchoring the MOF onto the chitosan beads requires further investigation. In the OPS method, free linkers were present in the solution, and it is probable that the chitosan surface itself was adequate to bind the initial MOF matrix complexes, resulting in the formation of the MOF film. This can have large implications, as the formation of a film within the larger structure of chitosan could results in a "perfect" coverage of MOF on the carrier, and additionally the MOF might add to the chemical or physical resistivity of the chitosan.

The presented method is an important steppingstone towards the development of renewable, advanced catalyst carriers suitable for a broad variety of applications in catalysis. This work opens the road to future applications including gas-phase chemical reactions and also in e.g., slurry-phase or liquid-phase reactions and alcohol oxidation or cascade alcohol oxidation-Knoevenagel condensation reactions, up to 200 °C, where diffusions of reagents or products limits the current applicability.[62–63] Additional to the highly porous nature of the beads, its easy functionalization can bind many different catalyst materials on its large surface, making them readily available and at the same time easy to separate from the final products.

Experimental Section

Chitosan bead Synthesis

Pure chitosan (CS) beads were synthesized by dissolving 3 wt% chitosan (98% purity, ≥75% deacetylated, Sigma–Aldrich) in a 1 wt% acetic acid (≥99%, glacial, ReagentPlus®, Sigma–Aldrich)/water solution. The chitosan was dissolved overnight under stirring at room temperature. The solution was drop-cast in liquid nitrogen with a BD microlance™ 3 needle, 0.8×40 mm in size (Figure 1). Tests were also made with lower concentrations of chitosan, as well as a smaller needle diameter (0.25×40 mm) to investigate the tunability of the bead size (Figure 3). Both variations lead to smaller beads. The formed beads were collected and freeze-dried for 24 h.

Synthesis of Platinum-Based UiO-67 (UiO-67-Pt)

2.5 mmol zirconium(IV) chloride (ZrCl4; ≥99%, Alfa Aesar) was combined with 2.3 mmol 1,1'-biphenyl-4,4'-dicarboxylic acid (BPDC; 97%, Sigma–Aldrich) and 0.26 mmol 2,2' bipyridine 5,5' dicarboxylic acid (BPYDC; 97%, Sigma–Aldrich) and dissolved in 0.65 mmol N,N dimethylformamide (DMF; 99% Alfa Aesar). When dissolved, 25.84 mmol benzoic acid (99.5%, Sigma–Aldrich), 3.44 mmol demi water, and 0.26 mmol potassium tetra chloroplatinate (II) (K2PtCl4; 99.9% Alfa Aesar) were added and heated to 95 °C for 72 h. The resulting crystalline powder was separated by centrifugation, washed twice with DMF, and twice with tetrahydrofuran (THF; 99.5% Alfa Aesar) before drying in an oven at 60 °C for 12 h and then at 150 °C for 24 h.

Chitosan/UiO-67 Bead Synthesis via One-Pot Synthesis (UiO 67-Pt-OPS@CS)

2.5 mmol ZrCl4, 2.3 mmol BPDC, 0.26 mmol BPYDC, 0.65 mmol DMF, 25.84 mmol benzoic acid 3.44 mmol ultrapure water, and 0.26 mmol K2PtCl4 were combined, as indicated in Figure 1b in light blue. When fully dissolved, pure chitosan beads were added to the solution and heated under stirring to 95 °C for 72 h. The resulting crystalline powder was separated from the composite beads by filtration, then the formed powder in the solution was centrifugation, washed twice with DMF, and twice with THF before drying in an oven at 60 °C for 12 h and then at 150 °C for 24 h. The beads were gently washed once with fresh DMF and twice with THF before drying them in a vacuum for 24 h.

Chitosan/UiO-67 Bead Synthesis via Post-Synthetic Functionalization (UiO-67-Pt-PSF@CS)

Pre-made chitosan beads and pre-impregnated UiO-67 powder MOF were mixed in DMF and heated under stirring to 95 °C for 72 h, as indicated in Figure 1c in light orange. For the incorporation of the metal precursor, platinum, 0.26 mmol potassium tetra chloroplatinate (II) (K_2PtCl_4) was added into to mixture so that the metal precursor could react with open BPYDC sites of UiO-67. The beads were gently washed once with fresh DMF and twice with THF before drying them in a vacuum for 24 h.

Attenuated Total Reflection-Infrared Spectroscopy

Attenuated total reflection-infrared (ATR-IR) spectroscopy was recorded on a Perkin Elmer Frontier spectrometer with a Mercury-Cadmium-Telluride (MCT) detector. The spectra were recorded from 600 to 4000 cm^{-1} and averaged over 32 scans with a resolution of 2 cm^{-1}. The spectra were post-processed using an automatic background correction and ATR correction in the Perkin Spectrum software.

Ultraviolet-Visible Spectroscopy

Ultraviolet-visible (UV-Vis) spectroscopy was used to measure the absorbance of the composite beads and powder MOF, using a Perkin-Elmer UV-Vis-NIR lambda 950S instrument with an integrating sphere in diffuse reflectance (DR) mode in the spectral range of 200 to 800 nm. The background was obtained by placing the sample holder filled with PTFE (400 μm grain size) at the sample position. The absorbance of the beads and the powder was determined by placing the sample at the entrance of the integration sphere.

Thermogravimetric Analysis

Thermogravimetric analysis (TGA) was measured on a Perkin Elmer 8000 instrument. Under a nitrogen atmosphere, the sample was heated to 200 °C at 10 °C/min. After that, the heating ramp was adapted to 5 °C/min from 200 °C up to 1000 °C, where the atmosphere was switched to oxygen and held for 10 min to burn off the remaining material of the sample.

Mercury (Hg) Porosimetry Analysis

Hg porosimetry experiments were performed at the Instituto de Catalisis y Petroleoquimica in Madrid, Spain by using a Micromeritics AutoPore IV 9510 mercury intrusion-extrusion equipment. The resolution, in terms of pore size is from 4 to 360 μm. Pore size distribution were determined at pressures up to 30000 psia.

Inductively Coupled Plasma Optical Emission Spectroscopy (ICP-OES) Analysis

ICP measurements were done using the Optima 8300DV from PerkinElmer. Prior to the measurements, samples were dissolved in an acid solution consisting of either 5% HNO3 or aqua regia.

Scanning Electron Microscopy

Scanning electron microscopy (SEM) images were recorded on a FEI Helios NanoLab G3 UC instrument. The beads were cut in half, using a single-edge stainless steel razor blade, to be able to also image the inner surface of the sample. External and internal morphologies were imaged by collecting secondary electrons (SE) with an Everhart–Thornley detector (ETD). Samples were loaded on aluminum stubs using a conductive carbon tape, and sputter-coated with 12 nm of Pt, before imagining, to avoid charging effects. The accelerating voltage was set to 2 kV and the current to 0.10 nA with a dwell time of 1 μs.

Supporting Information

Supplementary experimental data may be found in the Supporting Information.

Conflict of Interests

The authors declare no conflict of interest.

Data Availability Statement

The data that support the findings of this study are available from the corresponding author upon reasonable request.

[1] Q. Wang, D. Astruc, *Chem. Rev.* **2020**, *120*, 1438–1511.
[2] S. Dutt, A. Kumar, S. Singh, *Clean Technologies.* **2023**, *5*, 140–166.
[3] J. H. Cavka, S. Jakobsen, U. Olsbye, N. Guillou, C. Lamberti, S. Bordiga, K. P. Lillerud, *J. Am. Chem. Soc.* **2008**, *130*, 13850–13851.
[4] A. Dibenedetto, A. Angelini, P. Stufano, *J. Chem. Technol. Biotechnol.* **2014**, *89*, 334–353.
[5] K. Sumida, D. L. Rogow, J. A. Mason, T. M. McDonald, E. D. Bloch, Z. R. Herm, T. Bae, R. Long, *Chem. Rev.* **2012**, *112*, 724–781.
[6] C. Wang, Z. Xie, E. Kathryn, W. Lin, *J. Am. Chem. Soc.* **2011**, *133*, 13445–13454.

ChemPhysChem

Research Article
doi.org/10.1002/cphc.202400154

Chemistry Europe
European Chemical
Societies Publishing

[7] R. P. Ye, J. Ding, W. Gong, M. D. Argyle, Q. Zhong, Y. Wang, C. K. Russell, Z. Xu, A. G. Russell, Q. Li, M. Fan, Y. G. Yao, *Nat. Commun.* **2019**, *10*, 5698.

[8] J. Ye, J. K. Johnson, *Catal. Sci. Technol.* **2016**, *6*, 8392–8405.

[9] Y. L. Men, Y. Liu, Q. Wang, Z. H. Luo, S. Shao, Y.-B. Li, Y. X. Pan, *Chem. Eng. Sci.* **2019**, *200*, 167–175.

[10] E. S. Gutterød, A. Lazzarini, T. Fjermestad, G. Kaur, M. Manzoli, S. Bordiga, S. Svelle, K. P. Lillerud, E. Skúlason, S. Øien-Ødegaard, A. Nova, U. Olsbye, *J. Am. Chem. Soc.* **2020**, *142*, 999–1009.

[11] S. Kattel, B. Yan, J. G. Chen, P. Liu, *J. Catal.* **2016**, *343*, 115–126.

[12] E. S. Gutterød, S. Øien-ødegaard, K. Bossers, A. Nieuwelink, M. Manzoli, L. Braglia, A. Lazzarini, E. Borfecchia, S. Ahmadigoltapeh, B. Bouchev-reau, B. T. Lønstad-bleken, R. Henry, C. Lamberti, S. Bordiga, B. M. Weckhuysen, K. P. Lillerud, U. Olsbye, *Ind. Eng. Chem. Res.* **2017**, *56*, 13206–13218.

[13] A. J. McMichael, R. E. Woodruff, S. Hales, *Lancet* **2006**, *367*, 859–869.

[14] C. Vogt, E. Groeneveld, G. Kamsma, M. Nachtegaal, L. Lu, C. J. Kiely, P. H. Berben, F. Meirer, B. M. Weckhuysen, *Nat. Catal.* **2018**, *1*, 127–134.

[15] J. Liu, A. Zhang, M. Liu, S. Hu, F. Ding, C. Song, X. Guo, *J. CO2 Util.* **2017**, *21*, 100–107.

[16] A. Goeppert, M. Czaun, J.-P. Jones, G. K. S. Prakash, G. A. Olah, *Chem. Soc. Rev.* **2014**, *431*, 7995–8048.

[17] M. D. Porosoff, B. Yan, J. G. Chen, *Energy Environ. Sci.* **2016**, *9*, 62–73.

[18] J. Hagen, in *Industrial Catalysis: A Practical Approach*, Wiley-VCH, Weinheim, 3rd Ed., **2015**, pp. 211–238.

[19] V. G. Baldovino-medrano, M. T. Le, I. Van Driessche, E. Bruneel, C. Alcázar, M. T. Colomer, R. Moreno, A. Florencie, B. Farin, E. M. Gaigneaux, *Catal. Today* **2015**, *246*, 81–91.

[20] R. Bingre, B. Louis, P. Nguyen, *Catalysts* **2018**, *8*, 163.

[21] Q. Ma, T. Zhang, B. Wang, *Matter* **2022**, *5*, 1070–1091.

[22] D. Bazer-Bachi, L. Assié, V. Lecocq, B. Harbuzaru, V. Falk, *Powder Technol.* **2014**, *255*, 52–59.

[23] X. M. Liu, L. H. Xie, Y. Wu, *Inorg. Chem. Front.* **2020**, *7*, 2840–2866.

[24] Z. Su, Y. R. Miao, G. Zhang, J. T. Miller, K. S. Suslick, *Chem. Sci.* **2017**, *8*, 8004–8011.

[25] M. Lee, B. Y. Chen, W. Den, *Appl. Sci.* **2015**, *5*, 1272–1283.

[26] P. R. Yaashikaa, P. S. Kumar, S. Karishma, *Environ. Res.* **2022**, *212*, 113114.

[27] I. Vollmer, M. J. F. Jenks, M. C. P. Roelands, R. J. White, T. van Harmelen, P. de Wild, G. P. van der Laan, F. Meirer, J. T. F. Keurentjes, B. M. Weckhuysen, *Angew. Chem. Int. Ed.* **2020**, *59*, 15402–15423.

[28] N. Yan, X. Chen, *Nature* **2015**, *524*, 155–157.

[29] I. Younes, M. Rinaudo, *Mar. Drugs.* **2015**, *13*, 1133–1174.

[30] I. Aranaz, R. A. Alcántara, M. Concepción Civera, C. Arias, B. Elorza, A. H. Caballero, N. Acosta, *Polymer* **2021**, *13*, 3256.

[31] D. Chmolowska, N. Hamda, R. Laskowski, *J. Soils Sediments* **2017**, *17*, 299–305.

[32] M. Rinaudo, *Prog. Polym. Sci.* **2006**, *31*, 603–632.

[33] N. V. Majeti, R. Kumar, *React. Funct. Polym.* **2000**, *46*, 1–27.

[34] P. K. Dutta, J. Dutta, V. S. Tripathi, *J. Sci. Ind. Res.* **2004**, *63*, 20–31.

[35] N. Desai, D. Rana, S. Salave, R. Gupta, P. Patel, B. Karunakaran, A. Sharma, J. Giri, D. Benival, N. Kommineni, *Pharmaceutica* **2023**, *15*, 1313.

[36] E. Aghazadeh Asl, M. Pooresmaeil, H. Namazi, *Mater. Chem. Phys.* **2023**, *293*, 126933.

[37] K. B. Schnabl, L. D. B. Mandemaker, K. G. J. Nierop, O. V. B. Deen, D. D. Eefting, I. Vollmer, B. M. Weckhuysen, *ChemSusChem* **2023**, *16*, e202300585.

[38] Á. Molnár, *Coord. Chem. Rev.* **2019**, *388*, 126–171.

[39] D. J. Macquarrie, J. J. E. Hardy, *Ind. Eng. Chem. Res.* **2005**, *44*, 8499–8520.

[40] A. Balakrishnan, M. M. Jacob, N. Dayanandan, M. Chinthala, M. Ponnuchamy, D.-V. N Vo, S. Appunni, A. S. Gajendhran, *Mater Adv* **2023**, *4*, 2–28.

[41] Á. Molnár, *Coord. Chem. Rev.* **2019**, *388*, 126–171.

[42] H. Mousavi, *Int. J. Biol. Macromol.* **2021**, *186*, 1003–1166.

[43] R. Jayakumara, D. Menona, K. Manzoora, S. V. Naira, H. Tamurab, *Carbohydr. Polym.* **2010**, *82*, 227–232.

[44] G. Socrates in *Infrared and Raman Characteristic Group Frequencies: Tables and Charts*, 3rd ed., John Wiley & Sons, New York, **2004**, p. 94–104.

[45] A. Pankajakshan, M. Sinha, A. A. Ojha, S. Mandal, *ACS Omega* **2018**, *3*, 7832–7839.

[46] S. Øien, G. Agostini, S. Svelle, E. Borfecchia, K. A. Lomachenko, L. Mino, E. Gallo, S. Bordiga, U. Olsbye, K. P. Lillerud, C. Lamberti, *Chem. Mater.* **2015**, *27*, 1042–1056.

[47] O. Shekhah, *Materials* **2010**, *3*, 1302–1315.

[48] J. Liu, C. Wöll, *Chem. Soc. Rev.* **2017**, *46*, 5730–5770.

[49] L. D. B. Mandemaker, C. Jabbour, N. Nikolopoulos, J. M. Dorresteijn, M. Rivera-Torrente, B. M. Weckhuysen, *Adv. Mater. Interfaces* **2023**, *10*, 2201753.

[50] L. D. B. Mandemaker, M. Rivera-Torrente, G. Delen, J. P. Hofmann, M. Lorenz, A. Belianinov, B. M. Weckhuysen, *Chem. Eur. J.* **2020**, *26*, 691–698.

[51] M. Adlim, M. Abu Bakar, K. Y. Liew, J. Ismail, *J. Mol. Catal. A* **2004**, *212*, 141–149.

[52] L. Valenzano, B. Civalleri, S. Chavan, S. Bordiga, M. H. Nilsen, S. Jakobsen, K. P. Lillerud, C. Lamberti, *Chem. Mater.* **2011**, *23*, 1700–1718.

[53] X. Zhao, M. Xu, X. Song, X. Liu, W. Zhou, H. Wang, P. Huo, *Inorg. Chem.* **2022**, *61*, 1765–1777.

[54] X. Dong, Y. Lin, Y. Ma, *RSC Adv.* **2019**, *4*, 27674–27683.

[55] Q. Zhao, Z. Zhao, R. Rao, Y. Yang, S. Ling, F. Bi, X. Shi, *J. Colloid Interface Sci.* **2022**, *627*, 385–397.

[56] X. Jia, B. Zhang, C. Chen, X. Fu, Q. Huang, *Carbohydr. Polym.* **2021**, *253*, 117305.

[57] K. I. Hadjiivanov, D. A. Panayotov, M. Y. Mihaylov, E. Z. Ivanova, K. K. Chakarova, S. M. Andonova, N. L. Drenchev, *Chem. Rev.* **2021**, *121*, 1286–1424.

[58] I. K. D. Dimzon, T. P. Knepper, *Int. J. Biol. Macromol.* **2015**, *72*, 939–945.

[59] M. L. Duarte, M. C. Ferreira, M. R. Marvão, J. Rocha, *Int. J. Biol. Macromol.* **2002**, *31*, 1–8.

[60] A. López, M. J. Lis, F. M. Bezerra, M. Vilaseca, B. Vallés, R. Prieto, M. Simó, *J. Biomed. Sci. Eng.* **2019**, *12*, 377–390.

[61] D. K. Sannes, S. Øien-ØDegaard, E. Aunan, A. Nova, U. Olsbye, *Chem. Mater.* **2023**, *35*, 3793–3800.

[62] Z. Luo, H. Chen, S. Wu, C. Yang, J. Cheng, *Chemosphere* **2019**, *237*, 124493.

[63] S. Sadjadi, N. Abedian-Dehaghani, A. Heydari, M. M. Heravi, *Sci. Rep.* **2023**, *13*, 2797.